

Article

Photocatalytic Degradation of 2,4,6-Trichlorophenol by MgO–MgFe₂O₄ Derived from Layered Double Hydroxide Structures

Esthela Ramos-Ramírez ^{1,*} , Francisco Tzompantzi-Morales ², Norma Gutiérrez-Ortega ^{3,*} , Héctor G. Mojica-Calvillo ¹ and Julio Castillo-Rodríguez ² 

¹ Laboratory of Advanced Materials and Processes, Department of Chemistry, Division of Natural and Exact Sciences, University of Guanajuato, Guanajuato, Gto. 36050, Mexico; jhg.mojicacalvillo@ugto.mx

² Laboratory of Ecocatalysis, Department of Chemistry, Metropolitan Autonomous University, México City 09340, Mexico; fjtz@xanum.uam.mx (F.T.-M.); jarry-rasec@hotmail.com (J.C.-R.)

³ Laboratory of Environmental Engineering, Department of Civil Engineering, Division of Engineering, University of Guanajuato, Guanajuato, Gto. 36000, Mexico

* Correspondence: ramosre@ugto.mx (E.R.-R.); normagut@ugto.mx (N.G.-O.);
Tel.: +52-473-732-0006 (ext. 1457) (E.R.-R.); +52-473-732-0006 (ext. 2227) (N.G.-O.)

Received: 5 April 2019; Accepted: 14 May 2019; Published: 17 May 2019



Abstract: In recent years, the search for solutions for the treatment of water pollution by toxic compounds such as phenols and chlorophenols has been increasing. Phenols and their derivatives are widely used in the manufacture of pesticides, insecticides, paper, and wood preservers, among other things. Chlorophenols are partially biodegradable but not directly photodegradable by sunlight and are extremely toxic—especially 2,4,6-trichlorophenol, which is considered to be potentially carcinogenic. As a viable proposal to be applied in the treatment of water contaminated with 2,4,6-trichlorophenol, this paper presents an application study of the thermally activated Mg/Fe layered double hydroxides as photocatalysts for the mineralization of this contaminant. Activated Mg/Fe layered double hydroxides were characterized by X-ray diffraction, thermal analysis, N₂ physisorption, and scanning electron microscopy with X-ray dispersive energy. The results of the photocatalytic degradation of 2,4,6-trichlorophenol in aqueous solution showed good photocatalytic activity, with an efficiency of degradation of up to 93% and mineralization of 82%; degradation values which are higher than that of TiO₂-P25, which only reached 18% degradation. The degradation capacity is attributed to the structure of the MgO–MgFe₂O₄ oxides derived from double laminate hydroxide Mg/Fe. A path of degradation based on a mechanism of superoxide and hollow radicals is proposed.

Keywords: photocatalysis; Mg/Fe layered double hydroxides; coprecipitation; chlorophenols; mixed oxides; elimination; degradation

1. Introduction

Layered double hydroxides (LDH) or hydrotalcite-type compounds are a large class of natural and synthetic compounds of the anionic clay type [1,2]. These compounds are characterized by having a laminar structure with octahedral arrays of double metal hydroxides that generate a positive residual charge, which is neutralized by the presence of hydrated interlaminal anions [3–5]. Its structural formula is represented in a general way as $[M(II)_{1-x}M(III)_x(OH)_2]^{x+}[A_{x/n}^{n-}]_x \cdot mH_2O$, where M (II) and M (III) can be any divalent cation (Mg²⁺, Fe²⁺, Co²⁺, Zn²⁺, Cu²⁺, and Ni²⁺) or trivalent cation (Al³⁺, Fe³⁺, Cr³⁺, In³⁺, Ga³⁺, and Mn³⁺), respectively; A is any anion (CO₃²⁻, NO₃⁻, SO₄²⁻, Cl⁻, CrO₄²⁻, etc.) of n charge; x is the fraction of the trivalent cation (at the ratio of $x = M(III)/M(III)+M(II)$);

and m is the number of water molecules in the interlamellar space [6,7]. The properties of an LDH will depend on its structural characteristics and will determine the applications that can be given to them. A characteristic that is determinant for the use of an LDH is its profile of evolution of phases by thermal treatment, which allows dehydration, deionization, and dehydroxylation, with the subsequent formation of a variety of double and simple mixed metal oxides [8–10]. Among the main applications that have been found to thermally decompose the products of LDHs is heterogeneous catalysis [11–14]. More specifically, heterogeneous catalysis assisted by irradiation of ultraviolet and visible light as an advanced process of oxidation of recalcitrant and/or persistent organic molecules has become of interest as a potential application of LDHs [15,16]. Several advanced oxidation processes, such as O_3 /Ultraviolet (UV), O_3/H_2O_2 , UV/ H_2O_2 , Fenton, UV/Fenton, and UV/ TiO_2 , have been applied in wastewater as a treatment to mineralize many organic chemicals [17–21]. Within the persistent molecules that exist, interest in their degradation tends to increase by their toxicity and damage to the environment, as is the case for chlorophenols. Chlorophenols are aromatic compounds that are released into the environment in wastewater generated by the wood and petroleum processing industries, as well as the production of drugs, weapons, paper, textiles, and pesticides [22,23]. Most chlorophenols are considered highly toxic, depending on the nature and degree of ring substitution by chlorine. In general, the toxicity increases directly with the degree of chlorination. Specifically, 2,4,6-trichlorophenol tends to accumulate in the lipid tissues of several organisms, is mutagenic or co-mutagenic, and has been linked to cancer in animals, producing lymphomas and leukemia after consumption of contaminated food and water for long periods of time, and in high concentrations [24,25]. Specific studies on the degradation of 2,4,6-trichlorophenol using various technologies have included biological and physicochemical treatments. Specifically, biological treatments have been inefficient because 2,4,6-trichlorophenol is a molecule resistant to biodegradation, as well as being toxic to microorganisms. Physicochemical treatments such as thermal treatment and adsorption have the disadvantage of generating other dangerous compounds as a result of decomposition or generating residues with high concentrations of the contaminant, respectively [26–30]. Therefore, it is feasible to think of advanced oxidation processes as a more effective alternative for the destruction of this pollutant, such as ozone, hydrogen peroxide, photocatalysts, and even combinations of these. Among the semiconductors most used as photocatalysts in the degradation of 2,4,6-trichlorophenol are TiO_2 , Fe_2O_3 , CeO_2 , CuO , ZnO , ZrO , and Al_2O_3 , among others; they have been used either alone and mixed or doped, preferably with metals such as Ag, Au, Fe, Co, and Ni, to degrade the pollutant in a significant way [31–36]. The present work reports $MgO-MgFe_2O_4$ derived from layered double hydroxides Mg/Fe with band energy in the range of 2.28–2.47 eV, and its application in the degradation of 2,4,6-trichlorophenol in the aqueous phase using ultraviolet radiation as a source of light.

2. Results and Discussion

2.1. X-Ray Diffraction (XRD)

The X-ray diffraction patterns of the LDH are shown in Figure 1a. The three patterns are similar in relation to the position of the signals, but it is observed that crystallinity increases when the Mg/Fe ratio increases, with a tendency of LDHM1F < LDHM2F < LDHM3F, which is associated with a greater crystallinity produced by the decrease of Fe^{3+} within the brucite type network [$Mg(OH)_2$]. The characteristic signals are in the 2θ angles of 11.2 (003), 23.0 (006), 34.0 (012), 38.0 (015), 45 (018), 59.5 (110), and 61 (013), corresponding to the pyroaurite phase with the PDF card 25-0521 [2,37].

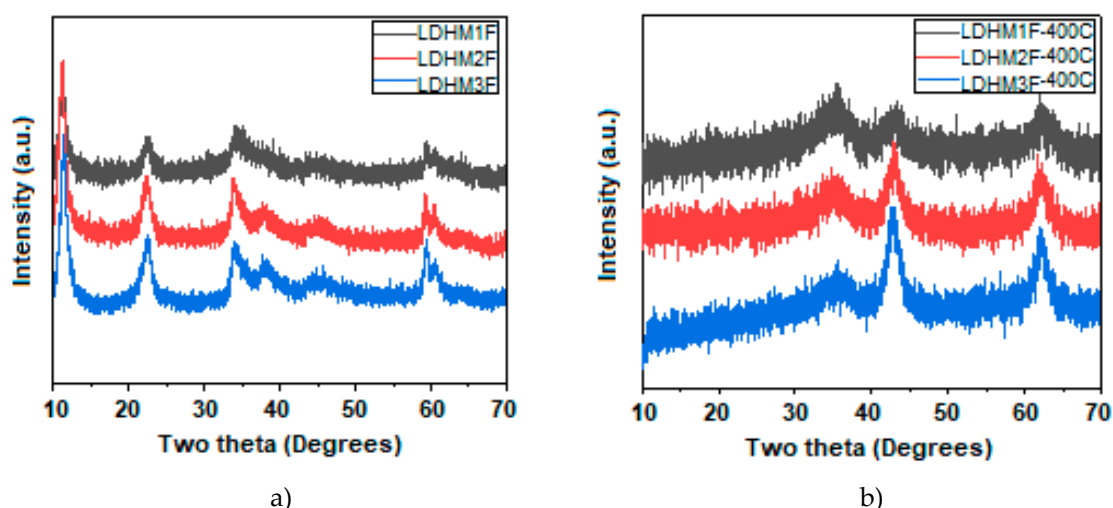


Figure 1. X-ray diffraction patterns of Mg/Fe layered double hydroxides. (a) Fresh and (b) thermally active at 400 °C.

In Figure 1b, the X-ray diffraction pattern of the layered double hydroxides, calcined at 400 °C, is shown. The presence of the crystalline phase of periclase (MgO) can be observed by characteristic signals in the 2θ angles of 36.80 (111), 42.85 (200), and 62.23 (220) (JCPDS-4-0829), showing a tendency to increase the crystallinity with respect to the Mg/Fe ratio. In the case of the solid LDHM1F, it is observed that at 400 °C the periclase phase has been formed but with a lower crystallinity, which is attributed to the fact that at these temperatures phase changes have occurred, although a higher temperature is required to favor crystallization. For the LDHM2F and LDHM3F solids, a better definition of the peaks is observed, which is associated with a better crystallinity, attributed to the fact that—having a lower amount of Fe—the MgO is more rapidly segregated. The above is associated with the thermal profile described in the following section, in which, in addition to the crystalline phases of MgO, the spinel phase (MgFe_2O_4) is segregated, which at 400 °C is amorphous. It is not identifiable by XRD.

2.2. Thermal Analysis: DTA and TGA

Figure 2 shows the differential thermal and thermogravimetric analysis of laminar double hydroxides. In the curve of the DTA (Figure 2a), in all cases an endothermic reaction is observed centered at 145 °C and associated with the elimination of interlaminar water molecules, followed by endothermic reactions centered at 290 °C and 350 °C, due to the dehydroxylation of the sheets and decomposition of the interlaminar carbonate. It can be observed that in the case of solid LDHM1F, the evolution to periclase (MgO) and to amorphous spinel (MgFe_2O_4) occurs at 330 °C. In the case of the solid LDHM2F and LDHM3F, the same profile of thermal decomposition is observed; however, it has a stability up to 350 °C, which is attributed to the greater crystallinity that they present as this favors the activation of the catalyst. The reactions associated with the thermal decomposition of LDH are shown in Equations (1)–(3). Thermal reactions of the LDH can be represented as:

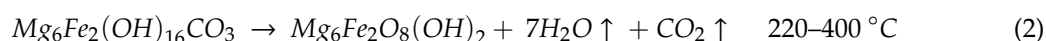
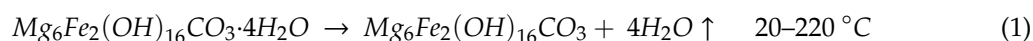


Figure 2b shows the weight loss profiles associated with the thermal decomposition of LDH, which are similar for all solids. In the first thermal decomposition reaction the solid LDHM1F reaches a weight loss of 21%, the solid LDHM2F a loss of 12.3%, and the solid LDHM3F a loss of 14.6%, which can be attributed to the desorption of water adsorbed on the porous surface of the solid and the water

occluded in the interlaminar space. The second weight loss is attributed to the partial dehydroxylation of the lamellar structure and the elimination of interlaminar carbonate ions; 16.86% for LDHM1F, 17.7% for LDHM2F, and 19.4% for LDHM3F. Finally, the final weight loss occurs when the solid is dehydroxylated completely, resulting in the collapse of the laminar structure with the subsequent segregation of the oxide phases, with losses of 7.72% for LDHM1F, 6.86% for LDHM2F, and of 9.69% for LDHM3F. The cumulative loss of transition from LDH precursors to the MgO and MgFe₂O₄ oxides was 45.58%, 36.86%, and 43.69% for LDHM1F, LDHM2F, and LDHM3F, respectively.

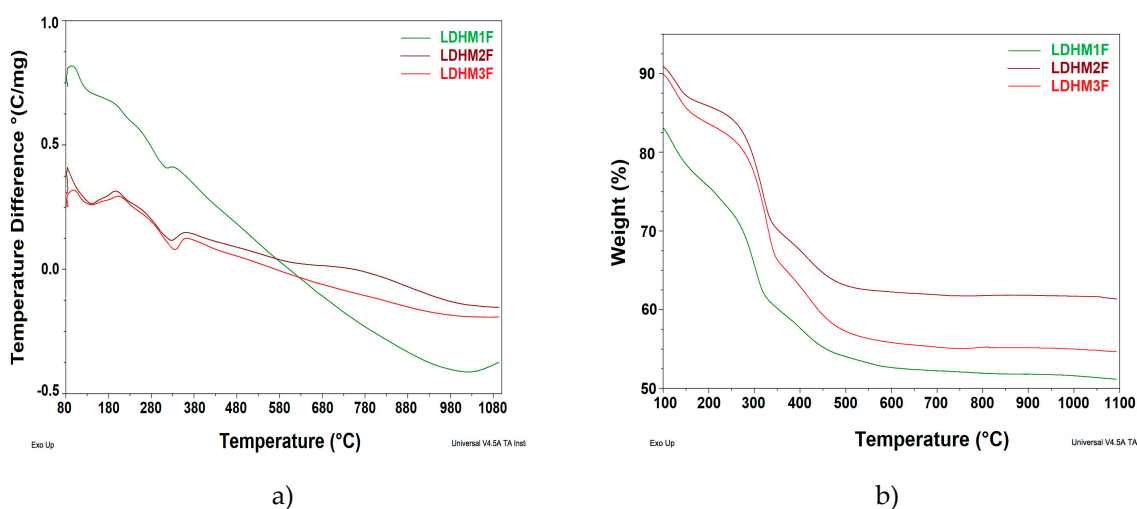


Figure 2. Thermal analysis of Mg/Fe layered double hydroxides. (a) Differential thermal analysis (DTA) and (b) thermogravimetric analysis (TGA).

2.3. Fourier Transformed Infrared Spectroscopy (FTIR)

The FTIR spectra of the LDH calcined at 400 °C are shown in Figure 3. The signals are similar for all solids. They present a band centered on 3550 cm⁻¹ that corresponds to the hydrogen bridge vibrations of the OH-OH₂ and H₂O-OH₂ types of the hydroxyl and water molecules remaining. A signal at 1640 cm⁻¹ corresponds to the H-OH vibration of the water. The band at 1360 cm⁻¹ is attributed to the carbonate ions remaining in the structure. The bands in the range of 750 to 500 cm⁻¹ are attributed to the metal-oxygen-metal stretch; specifically, the vibration frequency of 590 cm⁻¹ is attributed to the Fe-OH bond, the band at 630 cm⁻¹ corresponds to the vibration of O-Fe-O, and the band at 648 cm⁻¹ to the Mg-OH vibration.

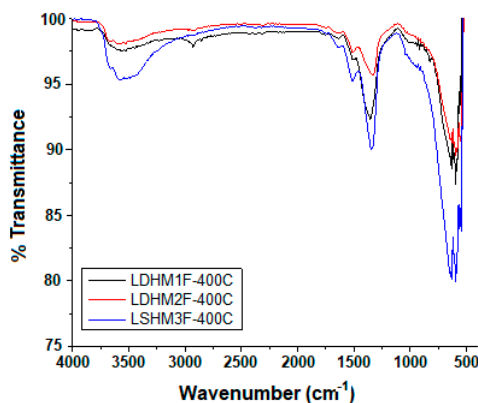


Figure 3. Fourier transformed infrared spectra of activated Mg/Fe layered double hydroxides.

2.4. Textural Analysis

The N₂ adsorption-desorption isotherms of LDH calcined at 400 °C are shown in Figure 4, showing that for all cases, type IV isotherms corresponding to mesoporous materials are presented according to the IUPAC classification. The isotherms at high values of relative pressure (P/P_0) did not show a horizontal tendency, which indicates that the nitrogen physisorption took place between the aggregates of particles that have a laminar morphology. Complementarily, the hysteresis cycles of the type H3 can be observed, which indicate the presence of pores of asymmetric size and asymmetrical shape.

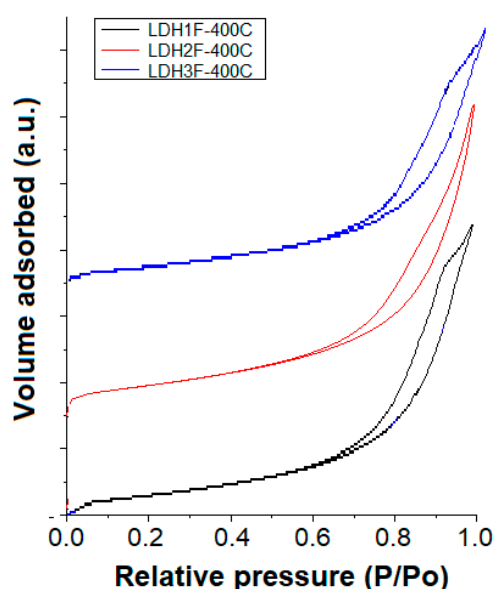


Figure 4. N₂ physisorption isotherms of activated Mg/Fe layered double hydroxides.

Table 1 shows the values of the specific areas determined by the Brunauer–Emmett–Teller (BET) method for the physisorption isotherms of N₂ of activated Mg/Fe layered double hydroxides, as well as the average pore diameter calculated by the Barrett, Joyner, and Halenda (BJH) method and the volume of the pores. It is observed that when the Mg/Fe ratio increases, there is a tendency to decrease the surface area, which is associated with the increase in the crystallinity of the solids and with the respective decrease in the pore size of the solids. The increase of area in the solids is because when the materials are calcined, the double structures collapse, and the pores of the tubular material expand (shape of the isotherm). The LDH with the highest specific area is the HTM1F-400 °C catalyst, which reaches specific areas close to 300 m²/g, which will favor the contact area of the photocatalyst with the pollutant.

Table 1. Textural properties of activated Mg/Fe layered double hydroxides.

Catalyst	BET Area (m ² /g)	Pore Diameter (nm)	Pore Volume (cm ³ /g)
LDHM1F-400 °C	282.2	8.72	0.0178
LDHM2F-400 °C	253.1	7.34	0.0391
LDHM3F-400 °C	248.9	6.30	0.0136

2.5. Scanning Electron Microscopy (SEM) with Energy-Dispersive X-Ray Spectroscopy (EDS)

Figure 5 shows the scanning microphotographs of activated layered double hydroxides. In the case of the solids LDHM2F-400 °C and LDHM3F-400 °C, crystals of heterogeneous size with numerous edges can be observed, in which the structure of stacked sheets can be seen, with crystallinity and very similar particle size, which will favor catalytic capacity for both solids. For the solid LDHM1F-400 °C,

the morphology looks similar, however, the particles are larger with the formation of aggregates of larger crystals, which hinders access to the active sites of the photocatalyst.

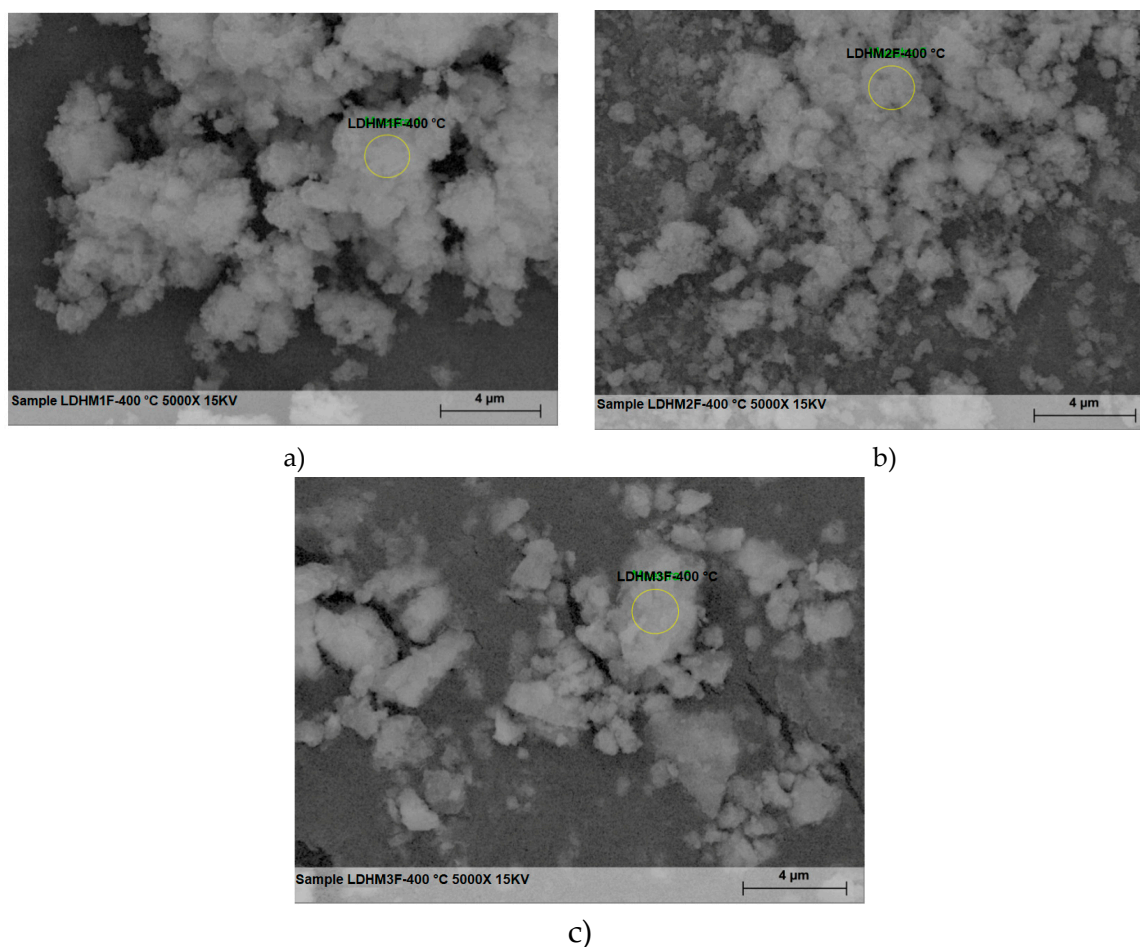


Figure 5. Scanning micrograph of activated layered double hydroxides at 5000x. (a) LDHM1F-400 °C, (b) LDHM2F-400 °C, (c) LDHM3F-400 °C.

The elemental composition of the surface of the activated LDH particles is shown in Figure 6, which contains the X-ray scattering energy spectra. As can be seen, the three solids have the same elements: Mg, Fe, and O, corresponding to the MgO and the spinel MgFe_2O_4 , but with different elemental molar ratios. Only in the case of solid LDHM1F-400 °C is a small amount of Na present, which was trapped in the LDH network at the time of synthesis. Regarding the metal molar ratio of Mg/Fe on the surface, this was 1, 1.97, and 2.1 for LDHM1F-400 °C, LDHM2 F-400 °C, and LDHM3F-400 °C, respectively, which for the first two solids corresponds to the theoretical molar ratio, while for the third solid a significant decrease of the same is observed.

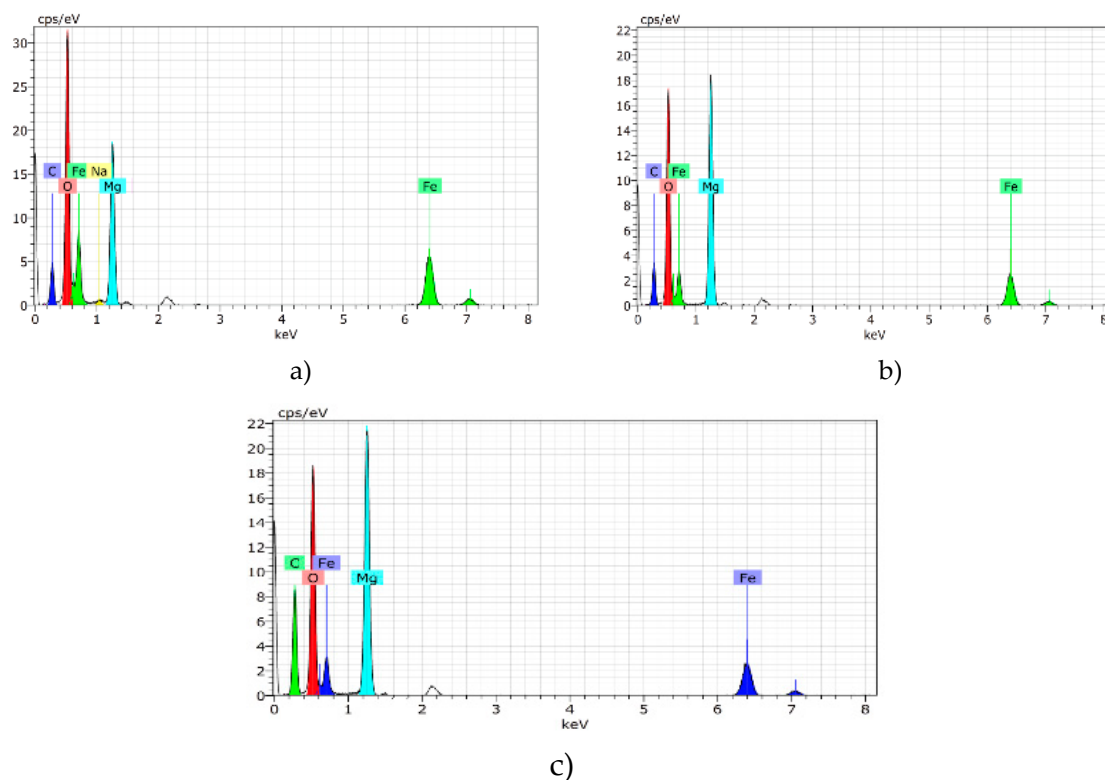


Figure 6. Energy-dispersive X-ray spectroscopy of activated layered double hydroxides at 5000x. (a) LDHM1F-400 °C, (b) LDHM2F-400 °C, (c) LDHM3F-400 °C.

2.6. Diffuse Reflectance Spectroscopy (DRS)

The evaluation of the band gap energy (E_g) for activated LDH was calculated using the Kubelka–Munk equation [$F(R) = (1-R)^2/2R$], where R is the converted reflectance (%) of the UV adsorption spectra, and these are reported in Figure 7. It can be observed that the values increase from 2.28 eV to 2.46 eV as a function of the Mg/Fe ratio, associated with the Fe^{3+} content. These results show that the content of Fe^{3+} in activated LDH materials modifies the semiconductor properties of solids due to a decrease in bandgap values by increasing the amount of Fe^{3+} , reaching values lower than 3.20 eV, corresponding to TiO_2 -P25.

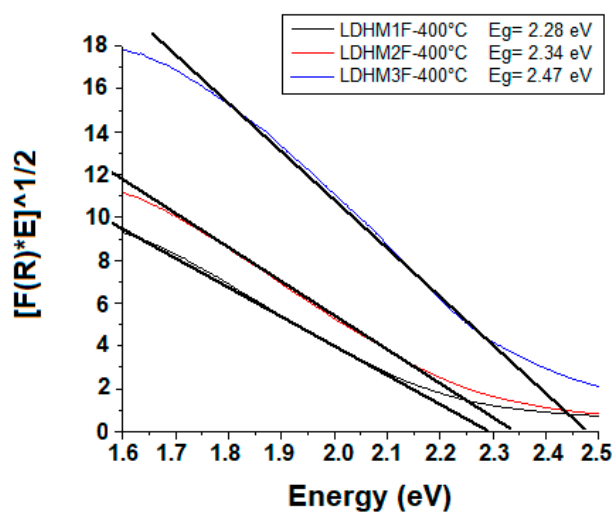


Figure 7. UV-vis-KM (Kubelka–Munk Method) spectra of activated Mg/Fe layered double hydroxides.

2.7. Photocatalytic Degradation of 2,4,6-Trichlorophenol

Figure 8 shows the ultraviolet-visible spectra of the degradation of a solution with a concentration of 80 parts per million (ppm), equivalent to 80 mg/L, of 2,4,6-trichlorophenol as a function of time, using activated LDH catalysts and TiO_2 at 400 °C as a reference control. The TiO_2 -P25 catalyst is used as a reference, since at the level of research and industrial application, it is used for the degradation of water polluting compounds due to its excellent stability, non-toxicity, being a semiconductor material with high photo-oxidation power, and low cost [19,36,38]. The 2,4,6-trichlorophenol spectra show three characteristic absorption bands, with the primary transition $\pi \rightarrow \pi^*$ assigned to the aromatic group between 208 and 220 nm, the secondary transition $\pi \rightarrow \pi^*$ at 243 nm due to the aromatic group, and the transition $n \rightarrow \pi^*$ that is attributed to the C–Cl link located at 311 nm [33,39]. In the case of activated LDH (Figure 8a–c), it can be observed that as time passes, the intensity of the three bands decreases, which is associated with the degradation of the 2,4,6-trichlorophenol molecule, until the complete disappearance of the bands of the secondary transition $\pi \rightarrow \pi^*$ at 243 nm occurs due to the aromatic group and the transition $\pi \rightarrow \pi^*$ of the C–Cl bond, as well as the decrease until almost the disappearance of the primary transition $n \rightarrow \pi^*$ assigned to the aromatic group at 240 min.

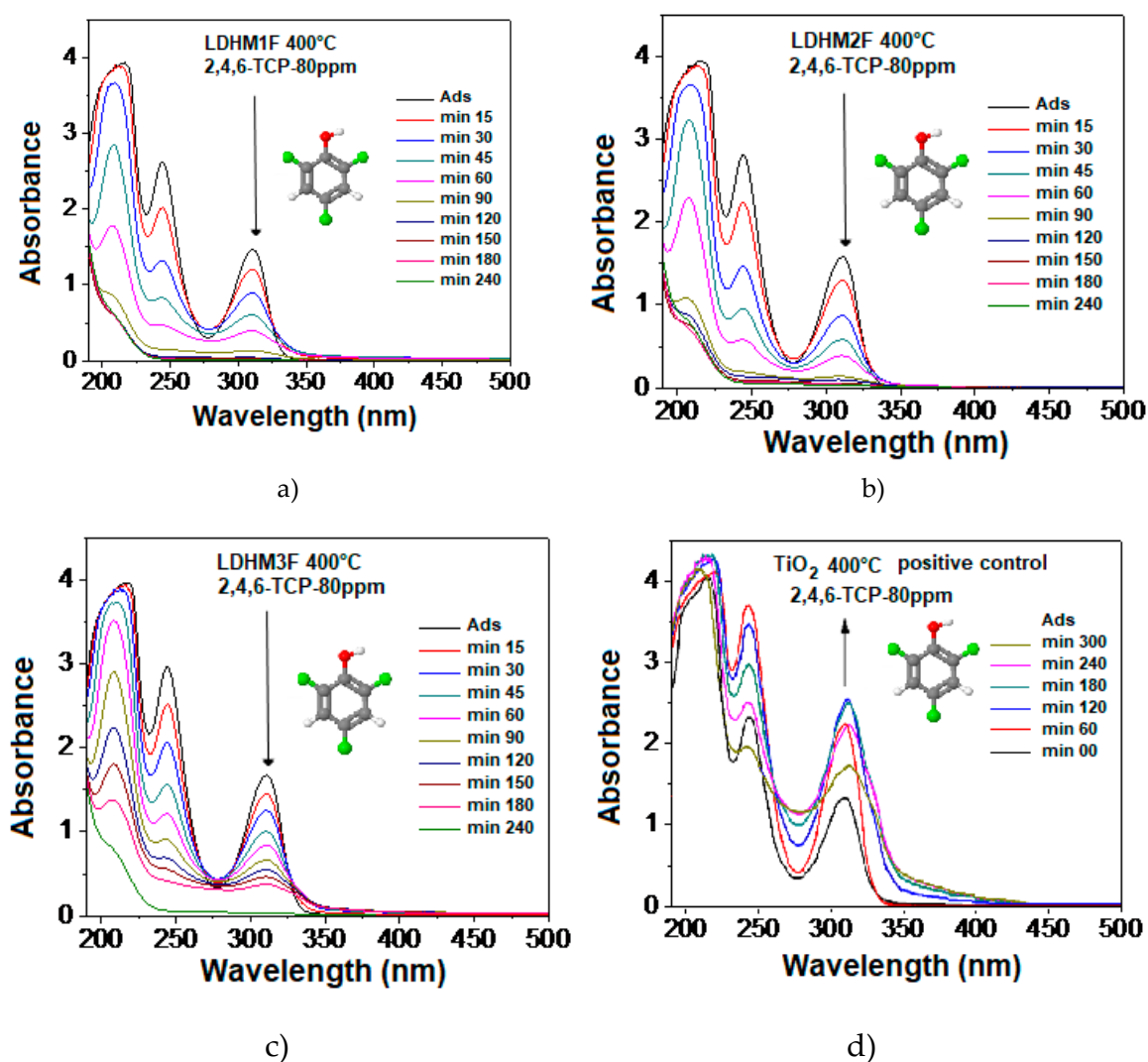


Figure 8. UV-vis spectra of the photocatalytic degradation of 2,4,6-TCP using Activated Lamellar Double Hydroxides (a) LDHM1F-400 °C, (b) LDHM2F-400 °C, (c) LDHM3F-400 °C, and (d) TiO_2 positive control.

In the case of the LDHM1F and LDHM2F catalysts, the decrease of the bands is very similar as a function of time, reaching degradation values higher than 90% at 90 min, while the LDHM3F catalyst at 90 min has only about 50% degradation, which is attributed to its band gap values of 2.34 and 2.47 eV. This is favored by the presence of Fe in the catalysts, requiring 240 min to reach values greater than 90% degradation of the entire organochlorine molecule. For TiO_2 used as a reference catalyst as a photocatalyst in the degradation of 2,4,6-trichlorophenol (Figure 8d), the intensity of the absorbance increases with the irradiation time, which is the opposite of the behavior of activated Mg/Fe LDH catalysts. The increase in the intensity of the signals is because the degradation of TiO_2 produces intermediates, which have higher absorptivity coefficients (This coefficient is proportional to the intensity in the absorbance), modifying the characteristic signals of 2,4,6-tetrachlorophenol at 245 and 310.5 nm. The intermediaries that are formed are mainly catechols, as well as benzoquinones and hydroxyquinones; all of them are compounds that preserve the aromatic ring increasing the signals between 200 and 225 nm.

Figure 9 shows the graph of the relative degradation rate of 80 ppm of 2,4,6-trichlorophenol with different catalysts. It can be corroborated that the photocatalysts show a good degradation of 2,4,6-trichlorophenol at 90 min, reaching 93% for LDHM2F-400 °C, 92% for LDHM1F-400 °C, and 55% for LDHM3F-400 °C—values higher than the 18% degradation of TiO_2 -P25-400 °C. For the catalysts LDHM1F-400 °C and LDHM2F-400 °C, the degradation behavior as a function of time is very similar, only showing a small difference at the beginning of the degradation process, whereas the catalyst of Mg/Fe = 1 ratio at 15 min has degraded the pollutant more quickly, but at 30 min, both catalysts reach the same speed, which at 90 min is slightly higher for the ratio catalyst Mg/Fe = 2.

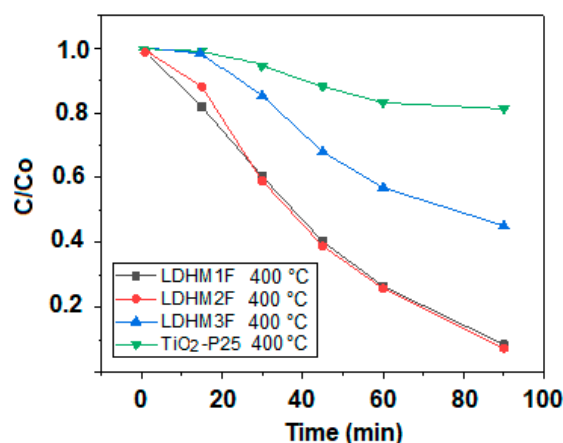


Figure 9. Relative photodegradation rate of 80 ppm of 2,4,6-trichlorophenol.

On the other hand, TiO_2 shows zero activity during the first 15 min, and then the degradation of the pollutant begins at a low speed, which allows it to reach 14% degradation at 60 min after the degradation process has begun, and only 18% at 90 min, showing a decrease in rate.

2.8. Kinetic Model Adjustment Study

Figure 10 shows the adjustment of the kinetic model of the relative degradation rate of 80 ppm of 2,4,6-trichlorophenol with the different catalysts, which corresponds to a pseudo-first-order degradation behavior in all cases—corresponding to the kinetic model of Langmuir–Hinshelwood, which is used to describe many photocatalytic reactions where the rate follows the kinetics of the pseudo-first-order considering steady state conditions [38,40].

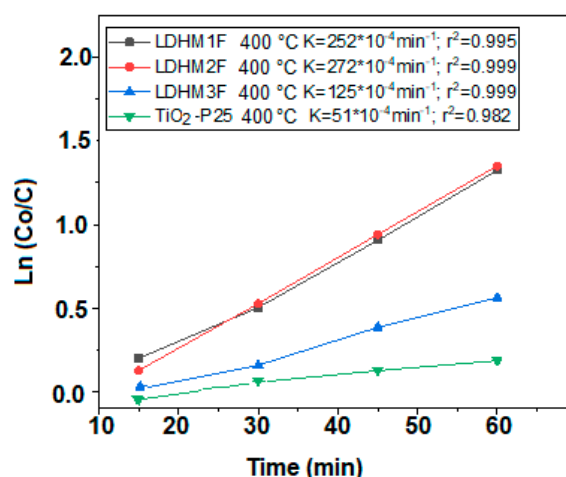


Figure 10. Pseudo-first-order degradation kinetics for 80 ppm of 2,4,6-trichlorophenol with activated layered double hydroxides and TiO₂-P25.

As seen in the Figure 10, the velocity constantly increases when the Mg/Fe molar ratio decreases, which is attributed to the role that Fe³⁺ plays in decreasing the bandgap value and allowing the photodegradation process to be carried out faster for the catalysts LDHM1F-400 °C and LDHM2F-400 °C, with the constant of apparent speed greater than $250 \times 10^{-4} \text{ min}^{-1}$ and half-lives of 25 min. These are much higher than those of TiO₂ of $51 \times 10^{-4} \text{ min}^{-1}$, with average lifetimes of 136 min.

2.9. Mineralization Study

The analysis of organic carbon (TOC) is shown in Figure 11, where it can be seen that the degradation of 2,4,6-trichlorophenol reaches values close to 80% for the catalysts LDHM1F-400 °C and LDHM2F-400 °C, reaching a greater mineralization using the LDHM2F-400 °C catalyst at 120 min, with values of 82%, which are higher than those reached by LDHM3F-400 °C and TiO₂-P25 of 61 and 29% at 120 min, respectively.

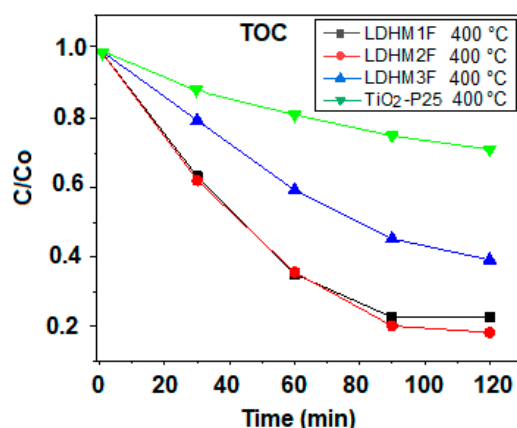


Figure 11. TOC removal during photodegradation of a 2,4,6-trichlorophenol solution.

Table 2 shows the values of the band gap, apparent speed constant, average flow time, percentage of degradation, and percentage of mineralization of the catalysts used in the degradation of 80 ppm of 2,4,6-trichlorophenol.

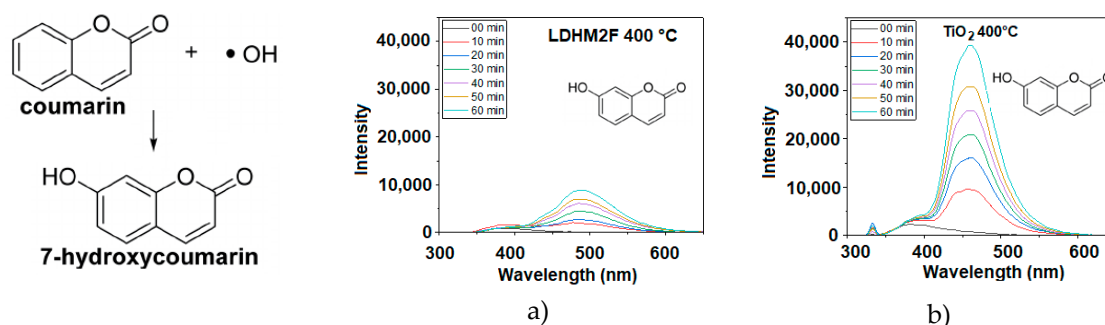
Table 2. Bandgap energy, specific area, apparent kinetic constant, half-life, percentage of degradation, and percentage of mineralization of activated layered double hydroxides.

Catalyst	Bandgap (eV)	$K_{app} \cdot 10^{-4}$ (min^{-1})	$t_{1/2}$ (min)	%Degradation (UV-Vis)	%Mineralization (TOC)
LDHM1F-400 °C	2.28	252	28	92	78
LDHM2F-400 °C	2.34	272	25	93	82
LDHM3F-400 °C	2.47	125	56	55	61
TiO ₂ -P25-400 °C	3.20	51	136	18	29

As can be seen, the LDHM1F and LDHM2 catalysts have very similar behaviors, however, the LDHM2F catalyst has a greater apparent speed constant, as well as a half-life of less than 25 min, 93% degradation and mineralization of 82%, which is why it can be considered as the catalyst with better photodegradation capacity for 2,4,6-trichlorophenol. This allowed LDHM2F-400 °C to be chosen to carry out studies on the possible mechanism of this photocatalytic reaction.

2.10. Detection of Hydroxyl Radicals (OH^\bullet)

In order to explore the mechanism of photocatalytic degradation, the possible formation of radicals was analyzed by fluorescence spectroscopy. For the detection of said radicals, coumarin was used as a molecule that captures the hydroxyl radicals, producing the hydroxyproduct 7-hydroxycoumarin [41], as shown in Figure 12.

**Figure 12.** Fluorescence spectra of coumarin employed in the detection of OH^\bullet generated by a photocatalyst without air bubbling: (a) LDHM2F-400 °C and (b) TiO₂-P25-400 °C.

The fluorescence spectra obtained with hydroxycoumarin exhibit a characteristic band of emission between 400 and 600 nm. In the case of the activated LDHM2F catalyst, the intensity of the signal is low, which implies that there is little presence of OH^\bullet radicals associated with the scarce formation of these in 60 min of reaction. On the other hand, in the case of the reference catalyst TiO₂-P25, an intense band associated with the production of hydroxycoumarin can be observed, due to the ability of the reference catalyst to produce hydroxyl radicals [42,43]. The above suggests that the activated LDHM2F catalyst does not favor the formation of OH^\bullet radicals.

2.11. Photocatalytic Evaluation of Superoxide Radicals ($\text{O}_2^{\bullet-}$)

As observed in Equation (4), when a semiconductor material is irradiated with energy greater than or equal to that of its forbidden bandwidth, the electrons are photoexcited from the valence band to the conduction band, with the probability of migrating to the surface of the semiconductor and reacting with bubbled oxygen (Equation (5)) during the reaction to produce superoxide radicals, which, like the hydroxyl radicals, have great oxidizing power for degrading the organic compound [44].





Using this photocatalytic foundation as a model to determine the formation of superoxide radicals in the process, the UV-Vis spectra were obtained in the photodegradation of 2,4,6-trichlorophenol. How the process develops in the presence of bubbled oxygen can be compared with a process with an absence of bubbling oxygen, where instead nitrogen gas is emitted, which is inert in the processes of photodegradation [45], as shown in Figure 13.

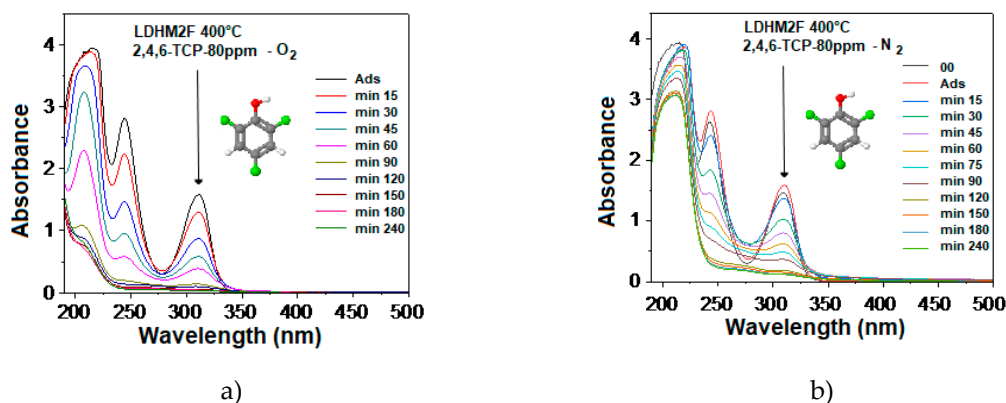


Figure 13. UV-Vis spectra in the photodegradation of 246-trichlorophenol in (a) the presence and (b) the absence of oxygen.

As can be seen, in the presence of O_2 the catalyst shows a good degradation capacity of 2,4,6-trichlorophenol, achieving the elimination of the signals of the vibrations of the functional groups C–Cl and C–OH, as well as a decrease of the CC and CH vibrations of the aromatic ring at 240 min. On the other hand, in the presence of N_2 it is observed that the catalyst is active in the partial degradation of the 2,4,6-trichlorophenol molecule, showing an almost total decrease of the vibrations of the functional groups C–Cl and C–OH, but only a small decrease in the CC and CH vibrations of the aromatic ring at 240 min.

As seen in Figure 14, the photocatalytic activity decreases by about 35% for the elimination of the OH and Cl functional groups in the absence of bubbled oxygen, according to the values of the apparent kinetic constants. The above confirms that the generation of superoxide radicals is determinant for the elimination of the functional groups, as well as for the degradation of the aromatic ring for the complete photodegradation of 2,4,6-trichlorophenol. The partial degradation of the 2,4,6-trichlorophenol molecule in the absence of oxygen suggests the participation of photogenerated voids (h^+) in the catalyst.

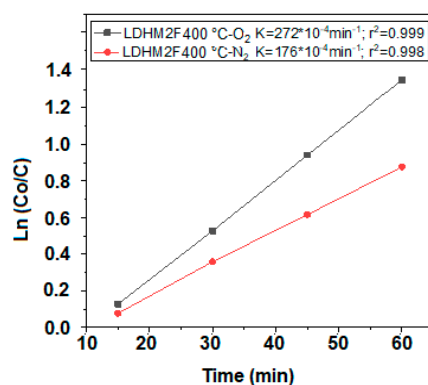


Figure 14. Kinetic constants in the photodegradation of 2,4,6-trichlorophenol in the presence and absence of oxygen.

2.12. Photocatalytic Evaluation of the Hole Trap (h^+)

The evaluation of the photocatalytic activity by gauging holes was evaluated using a model molecule of ammonium oxalate as a sacrificial agent [46–49]. Figure 15 shows the UV-Vis absorption spectra of the photodegradation of 2,4,6-trichlorophenol in the presence of ammonium oxalate with oxygen and nitrogen flow.

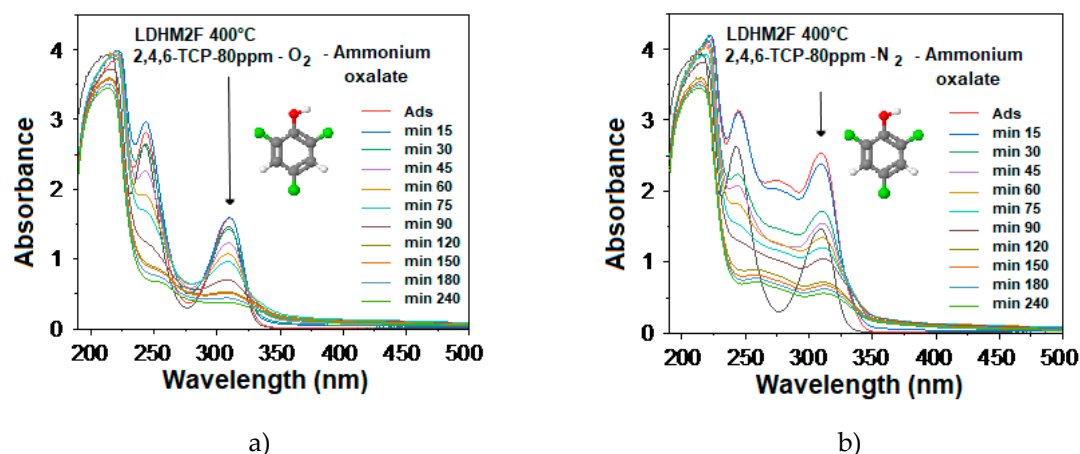


Figure 15. Absorption of UV-Vis for the photodegradation of 2,4,6-trichlorophenol in the presence of ammonium oxalate as a hole capture agent: (a) in the presence of oxygen; (b) in the presence of nitrogen.

According to the adsorption spectra, in the case of the photodegradation of 2,4,6-trichlorophenol in the presence of oxygen and ammonium oxalate, a reduction in the degradation of both the functional groups and the aromatic ring is observed. This confirms that the gaps that are formed in the LDHM2F-400 °C catalyst contribute in a significant way to the catalytic activity. On the other hand, in the case of the process of photodegradation in the absence of oxygen and in the presence of ammonium oxalate, it can be observed that the photodegradation process is completely modified, with the formation of a new band at the center at 275 nm. This is attributed to the formation of intermediaries which are identified by the signal of 2-chlorophenol, as well as a phase shift of the aromatic band attributed to the formation of phenol [27]. The above confirms that the catalytic activity of LDHM2F depends on the presence of voids, as well as the formation of superoxide radicals.

Table 3 shows the comparison of the apparent kinetic constants, percentage of degradation, and percentage of mineralization of the evaluation of the active species involved in the photodegradation of 2,4,6-trichlorophenol.

Table 3. Apparent kinetic constant, percentage of degradation, and percentage of mineralization of activated layered double hydroxides.

Catalyst	$K_{app} \times 10^{-4} \text{ (min}^{-1}\text{)}$	%Degradation (UV-Vis)	%Mineralization (TOC)
LDHM2F-400 °C with O ₂	252	91	77
LDHM2F-400 °C with N ₂	176	76	66
LDHM2F-400 °C-O ₂ with AO	87	47	20
LDHM2F-400 °C with N ₂ -AO	83	44	18

The catalytic activity related to the degradation of 2,4,6-trichlorophenol is decreased by more than 50% in the presence of ammonium oxalate and oxygen but is even more decreased in the absence of oxygen. As for mineralization, this is reduced by 77% in the absence of oxygen and in the presence of ammonium oxalate, which confirms that the degradation is partial, with the formation of intermediaries and not until mineralization has occurred. This behavior indicates that both the superoxide radicals and the holes (h^+) are the determinants, and both species contribute to the mechanism of photodegradation

until the mineralization of 2,4,6-trichlorophenol using the LDHM2F-400 °C catalyst. The results in Table 3 show that the oxidation of 2,4,6-trichlorophenol occurs first in the holes (h^+) photogenerated in the double-layered hydroxides under reconstruction and subsequently the intermediates are removed by further oxidation with superoxide radicals or other oxygen oxidizing species.

2.13. Possible 2,4,6-Trichlorophenol Degradation Mechanisms

Figure 16 shows a diagram of the proposed mechanism for the degradation of 2,4,6-trichlorophenol based on the properties of the catalysts and the different types of free radicals involved. As could be demonstrated in the fluorescence test for the detection of the generation of superoxide radicals, this is the main route involved in the degradation of the pollutant and, to a lesser extent, the holes. As observed in coumarin tests, photocatalysts do not favor the formation of hydroxyl radicals, so these free radicals do not contribute to the mechanism. Magnesium has a Pauling electronegativity of 1.31 eV and iron of 1.83 eV, so iron has a greater tendency to attract electrons to itself and transfer them to O_2 to generate the superoxide radical.

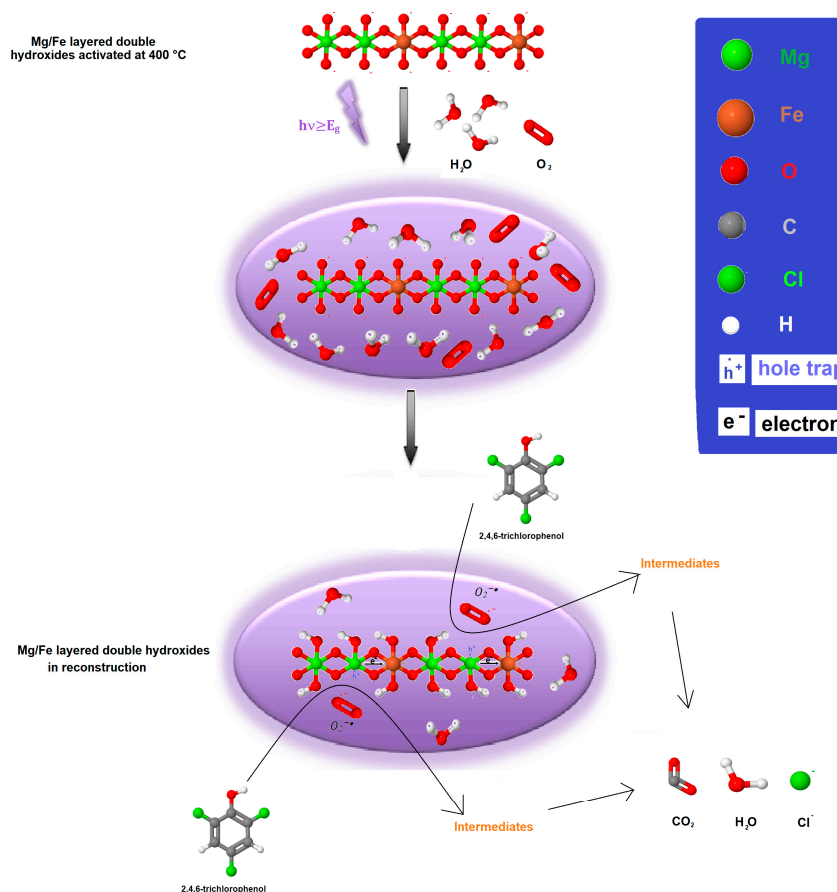


Figure 16. Possible routes for the degradation/mineralization of 2,4,6-trichlorophenol by activated layered double hydroxides.

As proposed in the possible degradation routes, this occurs when the activated layered double hydroxides, which are in the form of simple and mixed oxides, meet the aqueous medium with oxygen, which when irradiated produce an excess of electrons in the conduction band and positive gaps in the valence band, as shown in Equation (6).



On the other hand, electrons over the conduction band react with molecular oxygen, which acts as an electron acceptor to form superoxide radicals (Equation (7)).



The generated superoxide radicals can attack and oxidize 2,4,6-trichlorophenol (Equation (8)).



The final LDHMF catalytic precursor is recovered thanks to the memory effect, a property characteristic of the laminar double hydroxide materials [50–52]. Said precursor can be reactivated for a second cycle as a catalyst for the degradation of 2,4,6-trichlorophenol.

The degradation to the mineralization takes place thanks to the presence of superoxide radicals accompanied by the holes until the disappearance of the total organic carbon [32,53–56], implying a mechanism in which the superoxide radicals are carrying out the degradation of the aromatic ring simultaneously with the elimination of chlorine, since the formation of monochlorinated intermediates or phenols is not observed by the ultraviolet spectrum.

The catalyst with the highest photocatalytic activity is LDHM2F, whose pore volume value is higher compared to the LDHM1F-400 °C and LDHM3F-400 °C catalysts. This may indicate that there is enough separation between the laminar structures of the catalysts, promoting an improvement in the transfer of charges (e^{-} and h^{+}) by decreasing the recombination and, therefore, increasing the photocatalytic activity.

In the analysis by SEM, it is observed that the particle size of the LDHM2F-400 °C catalysts is lower than that of LDHM1F-400 °C, which indicates that, by the synthesis method used, the nucleation is different with the addition of Fe to the LDH. Being smaller particles, a lower percentage of conglomerates is obtained, suggesting that Fe increases directly in the LDH by modifying its electronegativity in such a way that a better transfer of charges is obtained, and with this the photocatalytic activity increases.

The main advantages of the activated layered double hydroxides are that they are not toxic, they can regenerate for continuous use, and they can be synthesized in an easy way, and without needing to be doped.

3. Materials and Methods

3.1. Obtaining Photocatalysts

3.1.1. Synthesis of Mg/Fe-Layered Double Hydroxide Catalytic Pre-Cursors of Ratios 1, 2, and 3

Layered double hydroxides with different Mg/Fe molar ratios were obtained by the coprecipitation method. The stoichiometric amounts of magnesium nitrate [$Mg(NO_3)_2 \cdot 6H_2O$], (Fermont, Lopez Mateos, Mexico), and iron nitrate [$Fe(NO_3)_3 \cdot 9H_2O$] (Fermont, Lopez Mateos, Mexico) were dissolved in water and subsequently coprecipitated at a pH of 11.5 with sodium hydroxide (NaOH) (Fermont, Lopez Mateos, Mexico). The coprecipitate was left and aged for 24 h, washed until it reached a pH of 9, and dried at 100 °C. The materials were identified as LDHM1F, LDHM2F, and LDHM3F, corresponding to the Mg/Fe = 1, 2, and 3 ratios.

3.1.2. Activation of Layered Double Hydroxides

The LDHs that were synthesized were thermally treated at 400 °C in an air atmosphere for 4 h for the formation of the mixed Mg/Fe oxides and were identified as LDHM1F-400 °C, LDHM2F-400 °C, and LDHM3F-400 °C.

3.2. Physicochemical Characterization of Catalytic Pre-Cursors and Catalysts

The materials were characterized by physicochemically fresh and calcined. To corroborate the present crystalline phase, X-ray diffraction was performed on a Siemens D500 powder diffractometer (University of Guanajuato, Guanajuato, Mexico) with CuK α radiation, a graphite crystal monochromator with a step of 2θ equal to 0.02 s^{-1} , and a counting time of 9 s per point. The thermal analyses were carried out in a TA Instruments Thermoanalyzer (University of Guanajuato, Guanajuato, Mexico) at a heating rate of $10\text{ }^{\circ}\text{C}/\text{min}$ in an air atmosphere, at a speed of $100\text{ mL}/\text{min}$ and using α -alumina as a reference. The infrared spectra with Fourier transform were obtained in a Bruker model Tensor 27 Hyperion 7000 (University of Guanajuato, Guanajuato, Mexico) with a resolution of 4 cm^{-1} and 20 scans, from 400 to 4000 cm^{-1} , and the samples were prepared by dilution with KBr. The nitrogen adsorption-desorption isotherms were determined in TriStar Micromeritics equipment (University of Guanajuato, Guanajuato, Mexico), with the samples previously dried at $100\text{ }^{\circ}\text{C}$ for 24 h, with a degassing at $150\text{ }^{\circ}\text{C}$, and a vacuum pressure of up to 0.5 mmHg . The BET model was used to obtain the specific area. Scanning electron microscopy analysis was performed on a Seizz 1550VP microscope with field emission, with Oxford EDS equipment (University of Guanajuato, Guanajuato, Mexico) with an opening of $30.0\text{ }\mu\text{m}$ and a width of 3.1 mm . The band gap energy of the photocatalysts was calculated from the ultraviolet absorption spectra coupled with an integrating sphere (diffuse reflectance) in a UV-Vis Recording S UV2401 Shimadzu instrument (University of Guanajuato, Guanajuato, Mexico), and using the Kubelka–Munk theory, which consists of plotting the energy of the photon against the square root of the Kubelka–Munk function multiplied by the energy of the photon and extrapolating the linear part with the abscissa axis.

3.3. Evaluation of the Photocatalytic Activity in the Degradation of 2,4,6-Trichlorophenol

3.3.1. Degradation of 2,4,6-Trichlorophenol

The photocatalytic degradation capacity of 2,4,6-trichlorophenol using activated LDH was determined under the following conditions: standard 200 ml solution at a concentration of 80 ppm of 2,4,6-trichlorophenol (Sigma-Aldrich, St. Louis, MO, USA), in a Batch reactor at a controlled temperature of $25\text{ }^{\circ}\text{C}$ with constant magnetic stirring of 700 rpm, with a flow of air of $2\text{ mL}/\text{s}$ and a UV light irradiation of 254 nm, and an emission of $2.5\text{ mW}/\text{cm}^2$ generated by a Pen-Ray UV lamp inserted in a tube of quartz. The photoactivity of all materials was determined by using $1\text{ g}/\text{L}$ of photocatalyst. To determine the adsorption phenomena effect, the suspension was stirred at 800 rpm under airflow in dark conditions for 1 h; after that, an aliquot was collected, and the reaction was started by turning on the UV lamp that was kept on for 240 min while stirring. Additionally, a sample of 2,4,6-trichlorophenol solution was subjected to photolysis in the absence of any catalyst to determine the effect of the radiation on the contaminant. In addition, for the comparison against a reference photocatalyst, commercial TiO_2 -P25 was used. In all cases, the process of degradation of 2,4,6-trichlorophenol was monitored using an aliquot sample of the reactor, with the subsequent quantification of this in a UV-Vis Cary 100 spectrophotometer (Metropolitan Autonomous University, Mexico City, Mexico) at a wavelength of 310.5 nm. The aliquots were collected at 15-minute intervals for 240 min, and in order to separate the solid catalyst from the aqueous solution, the aliquots were filtered using a nitrocellulose membrane with a pore size of $0.22\text{ }\mu\text{m}$ (Millipore Corporation, Burlington, Massachusetts, Estados Unidos). The amount of total organic carbon present in the irradiated solution was determined in a TOC-V-CSH/CSN Shimadzu 5000 TOC (Metropolitan Autonomous University, Mexico City, Mexico) to corroborate the degradation of the molecule until mineralization.

3.3.2. Detection of Hydroxyl and Superoxide Radicals and Study of the Hole Trap

A dilute aqueous solution ($2 \times 10^{-3}\text{ M}$) of coumarin (Sigma-Aldrich, St. Louis, MO, USA) was prepared, in which 200 mL of solution and 200 mg of photocatalyst to be analyzed were poured into a Batch reactor. TiO_2 -P25 was used as the reference material. As above, the study was carried

out in the absence of a photocatalyst (Photolysis) to observe the possible production of hydroxyl radicals with and without a photocatalyst. Once this was done, the solution was irradiated with UV light for 1 h with a Pen-Ray lamp ($\lambda = 254 \text{ nm}$ and $I_0 = 4.4 \text{ mWcm}^{-2}$) under conditions of constant stirring, oxygen bubbling, and temperature (800 rpm, 1 mL/s, and 25 °C, respectively), extracting 3 mL aliquots at 10 min intervals. Finally, the fluorescence emission spectra in the irradiated solution were analyzed by photoluminescence in a Fluorescence spectroscopy Scinco FS-2 spectrometer (Metropolitan Autonomous University, Mexico City, Mexico), a wavelength of 320 nm, and the results obtained with the synthesized materials and photolysis were compared with those obtained using the reference solid $\text{TiO}_2\text{-P25}$.

3.3.3. Photocatalytic Evaluation of Hole Capture with Ammonium Oxalate as a Sacrificial Agent

The photocatalytic reaction was monitored with the material with the highest photodegradation (HTM2F-400 °C) in the presence of ammonium oxalate (Sigma-Aldrich, St. Louis, MO, USA), and with oxygen and nitrogen flow. An aqueous solution of 246-TCF at 80 ppm was used, and 1 g/L of the photocatalyst with higher activity and a concentration of 0.004 M of ammonium oxalate were poured into a reactor. The solution was irradiated with UV light, maintaining the conditions of constant stirring, bubbling of nitrogen/oxygen, and temperature (800 rpm, 1 mL/s, and 25 °C, respectively), while extracting aliquots of 3 mL to be analyzed by UV-Vis spectroscopy.

4. Conclusions

The results of the present work show that layered double hydroxides of different Mg/Fe molar ratio can be synthesized by the coprecipitation method, which have a hydrotalcite crystalline structure, and which when calcined at 400 °C evolve to a crystalline phase of periclase and an amorphous phase of spinel, with Type IV isotherms characteristic of mesoporous materials and specific areas between 273.9 and 248.9 m^2/g . Layered double hydroxides activated at 400 °C have E_g values ranging from 2.28 to 2.47, which are lower values than TiO_2 , so they have better semiconductor properties. These photocatalysts have good photocatalytic activity, with degradation efficiencies for 2,4,6-trichlorophenol of 93% LDHM2F-400 °C > 92% LDHM1F-400 °C > 55% LDHM3F-400 °C > 18% $\text{TiO}_2\text{-P25-400 °C}$ in less than 90 minutes. Therefore, it is concluded that the most active catalysts are LDHM2FI-400 °C and LDHM1F-400 °C, which present a greater amount of iron in the structure and which reach mineralization values of up to 82%. The degradation mechanism proposed for the photodegradation of 2,4,6-trichlorophenol considers that the degradation occurs first in the photogenerated holes in the layered double hydroxides under reconstruction and then the intermediates are removed by further oxidation with the superoxide radicals or other oxidizing species of oxygen. These photocatalysts obtained from Mg/Fe layered double hydroxides are promising for the photodegradation of recalcitrant chlorinated compounds.

Author Contributions: Conceptualization, E.R.-R. and N.G.-O.; methodology, E.R.-R., H.G.M.-C., and J.C.-R.; software, J.C.-R.; validation, F.T.-M.; formal analysis, F.T.-M., H.G.M.-C., and J.C.-R.; investigation, F.T.-M.; resources, H.G.M.-C.; data curation, N.G.-O.; writing—original draft preparation, E.R.-R.; writing—review and editing, N.G.-O. and E.R.-R.; funding acquisition, E.R.-R.

Funding: This research received no external funding. Funding was received from the resources of the University of Guanajuato.

Acknowledgments: We would like to especially thank the Directorate for Research and Postgraduate Support (DAIP) at the University of Guanajuato for their support in developing this project. Also, we thank the University of Guanajuato-CONAcYT National Laboratory SEM-EDS. Additionally, we thank the CONAcYT for the graduate scholarship and UAM-I for technical support.

Conflicts of Interest: The authors declare no conflict of interest.

References

1. Miyata, S. Physico-chemical properties of synthetic hydrotalcites in relation to composition. *Clays Clay Miner.* **1980**, *28*, 50–56. [[CrossRef](#)]
2. Mills, S.J.; Christy, A.G.; Génin, J.M.R.; Kameda, T.; Colombo, F. Nomenclature of the hydrotalcite supergroup: Natural layered double hydroxides. *Mineral. Mag.* **2012**, *76*, 1289–1336. [[CrossRef](#)]
3. Roelofs, J.C.A.A.; Bokhoven, J.A.; Dillen, A.J.; Geus, J.W.; Jong, K.P. The Thermal Decomposition of Mg±Al Hydrotalcites: Effects of Interlayer Anions and Characteristics of the Final Structure. *Chem. Eur. J.* **2002**, *8*, 5571–5579. [[CrossRef](#)]
4. Nguyen, H.K.D.; Nguyen, H.V.; Nguyen, V.A. Effect of synthetic conditions on the structure of mesoporous Mg-Al-Co hydrotalcite. *J. Mol. Struct.* **2018**, *1171*, 25–32. [[CrossRef](#)]
5. Sikander, U.; Sufian, S.; Salam, M.A. A review of hydrotalcite based catalysts for hydrogen production systems. *Int. J. Hydrogen Energy* **2017**, *42*, 19851–19868. [[CrossRef](#)]
6. Cavani, F.; Trifiro, F.; Vaccari, A. Hydrotalcite-type anionic clays: Preparation, properties and applications. *Catal Today* **1992**, *11*, 173–301. [[CrossRef](#)]
7. Othman, M.R.; Helwani, Z.; Martunus, W.J.N. Synthetic hydrotalcites from different routes and their application as catalysts and gas adsorbents: A review. *Appl. Organomet. Chem.* **2009**, *23*, 335–346. [[CrossRef](#)]
8. Yahyaoui, R.; Sanchez, P.E.; Pérez, L.A.; Nahdi, K.; Criado, J.M. Synthesis, characterization and combined kinetic analysis of thermal decomposition of hydrotalcite (Mg₆Al₂(OH)₁₆CO₃·4H₂O). *Thermochim. Acta* **2018**, *667*, 177–184. [[CrossRef](#)]
9. Vágvölgyi, V.; Palmer, S.J.; Kristóf, J.; Frost, R.L.; Horváth, E. Mechanism for hydrotalcite decomposition: A controlled rate thermal analysis study. *J. Colloid Interface Sci.* **2008**, *318*, 302–308. [[CrossRef](#)]
10. Mokhtar, M.; Inayat, A.; Ofili, J.; Schwieger, W. Thermal decomposition, gas phase hydration and liquid phase reconstruction in the system Mg/Al hydrotalcite/mixed oxide: A comparative study. *Appl. Clay Sci.* **2010**, *50*, 176–181. [[CrossRef](#)]
11. Parida, K.M.; Sahoo, M.; Singha, S. Synthesis and characterization of a Fe(III)-Schiff base complex in a Zn-Al LDH host for cyclohexane oxidation. *J. Mol. Catal. A Chem.* **2010**, *329*, 7–12. [[CrossRef](#)]
12. Védrine, J.C. Heterogeneous Catalysis on Metal Oxides. *Catalysts* **2017**, *7*, 341. [[CrossRef](#)]
13. Baloyi, J.; Ntho, T.; Mom, J. Synthesis and application of pillared clay heterogeneous catalysts for wastewater treatment: A review. *RSC Adv.* **2018**, *8*, 5197. [[CrossRef](#)]
14. Prasad, C.; Tang, H.; Liu, W. Magnetic Fe₃O₄ based layered double hydroxides (LDHs) nanocomposites (Fe₃O₄/LDHs): Recent review of progress in synthesis, properties and applications. *J. Nanostruct. Chem.* **2018**, *8*, 393–412. [[CrossRef](#)]
15. Moma, J.; Baloyi, J.; Ntho, T. Synthesis and characterization of an efficient and stable Al/Fe pillared clay catalyst for the catalytic wet air oxidation of phenol. *RSC Adv.* **2018**, *8*, 30115. [[CrossRef](#)]
16. Valencia-Lopez, C.D.; Zafra-Calvo, M.; Martín de Vidales, M.J.; Blanco-Gutierrez, V.; Atanes-Sanchez, E.; Merayo, N.; Fernandez-Martinez, F.; Nieto-Marquez, A.; Dos santos-Garcia, J. Synthesis of NiFe₂O₄-LDH Composites with High Adsorption and Photocatalytic Activity for Methyl Orange Degradation. *Inorganics* **2018**, *6*, 98. [[CrossRef](#)]
17. Li, Z.; Chen, H.; Liu, W. Full-Spectrum Photocatalytic Activity of ZnO/CuO/ZnFe₂O₄ Nanocomposite as a PhotoFenton-Like Catalyst. *Catalysts* **2018**, *8*, 557. [[CrossRef](#)]
18. Descorme, C. Catalytic wastewater treatment: Oxidation and reduction processes. Recent studies on chlorophenols, Claude Descorme. *Catal Today* **2017**, *297*, 324–334. [[CrossRef](#)]
19. Lazar, M.A.; Varghese, S.; Nair, S.S. Photocatalytic Water Treatment by Titanium Dioxide: Recent Updates. *Catalysts* **2012**, *2*, 572–601. [[CrossRef](#)]
20. Pi, Y.; Wang, J. Pathway of the ozonation of 2,4,6-trichlorophenol in aqueous solution. *Front. Environ. Sci. Eng. China* **2007**, *1*, 179–183. [[CrossRef](#)]
21. Yan, Y.; Wu, X.; Zhang, H. Catalytic wet peroxide oxidation of phenol over Fe₂O₃/MCM-41 in a fixed bed reactor. *Sep. Purif. Technol.* **2016**, *171*, 52–61. [[CrossRef](#)]
22. Honda, M.; Kannan, K. Biomonitoring of chlorophenols in human urine from several Asian countries, Greece and the United States. *Environ. Pollut.* **2018**, *232*, 487–493. [[CrossRef](#)]
23. Badanthadka, M.; Mehendale, H.M. Chlorophenols. In *Encyclopedia of Toxicology*, 3rd ed.; Elsevier: Amsterdam, The Netherlands, 2014; pp. 896–899. [[CrossRef](#)]

24. Mostafalou, S.; Abdollahi, M. Pesticides: An update of human exposure and toxicity. *Arch. Toxicol.* **2017**, *91*, 549–599. [[CrossRef](#)]
25. Michałowicz, J. Pentachlorophenol and its derivatives induce oxidative damage and morphological changes in human lymphocytes (in vitro). *Arch. Toxicol.* **2010**, *84*, 379–387. [[CrossRef](#)]
26. Khorsandi, H.; Ghochlavi, N.; Aghapour, A.A. Biological Degradation of 2,4,6-Trichlorophenol by a Sequencing Batch Reactor. *Environ. Process.* **2018**, *5*, 907–917. [[CrossRef](#)]
27. Yi, A.; Feng, Y.; Du, Z.; Li, H. Mechanism of 2, 4, 6-Trichlorophenol Degradation in Microbial Fuel Cells System with Microbe Isolated from Submarine Sediment. *Int. J. Electrochem. Sci.* **2015**, *10*, 1459–1468.
28. Krishnaiah, D.; Anisuzzaman, S.M.; Bono, A.; Sarbatly, R. Adsorption of 2,4,6-trichlorophenol (TCP) onto activated carbon. *J. King Saud Univ. Sci.* **2013**, *25*, 251–255. [[CrossRef](#)]
29. Zhao, P.; Liu, X.; Tian, W.; Yan, D.; Sun, X.; Lei, X. Adsorbilization of 2,4,6-trichlorophenol from aqueous solution by surfactant intercalated ZnAl layered double hydroxides. *Chem. Eng. J.* **2015**, *279*, 597–604. [[CrossRef](#)]
30. Saritha, P.; Suman, D.S.; Aparna, C.; Vijaya, P.N.; Himabindu, V.; Anjaneyulu, Y. Degradative Oxidation of 2,4,6 Trichlorophenol Using Advanced Oxidation Processes—A Comparative Study. *Water Air Soil Pollut.* **2009**, *200*, 169–179. [[CrossRef](#)]
31. Kashyap, J.; Riaz, U. Facile synthesis of novel polypyrrole dispersed AgFeO₂ nanohybrid with highly efficient photocatalytic activity towards 2,4,6-trichlorophenol degradation. *RSC Adv.* **2018**, *8*, 13218–13225. [[CrossRef](#)]
32. Benbachir, H.; Gaffour, H.; Mokhtari, M. Photodegradation of 2,4,6-trichlorophenol using natural hematite modified with chloride of zirconium oxide. *React. Kinet. Mech. Catal.* **2017**, *122*, 635–653. [[CrossRef](#)]
33. Pino-Chamorro, J.Á.; Ditrói, T.; Lente, G.; Fábíán, I. A detailed kinetic study of the direct photooxidation of 2,4,6-trichlorophenol. *J. Photochem. Photobiol. A* **2016**, *330*, 71–78. [[CrossRef](#)]
34. Chaliha, S.; Bhattacharyya, K.G. Wet oxidative method for removal of 2,4,6-trichlorophenol in water using Fe(III), Co(II), Ni(II) supported MCM41 catalysts. *J. Hazard. Mater.* **2008**, *150*, 728–736. [[CrossRef](#)] [[PubMed](#)]
35. Yang, J.; Chen, H.; Gao, J.; Yan, T.; Zhou, F.; Cuin, S.; Bi, W. Synthesis of Fe₃O₄/g-C₃N₄ nanocomposites and their application in the photodegradation of 2,4,6-trichlorophenol under visible light. *Mater. Lett.* **2016**, *164*, 183–189. [[CrossRef](#)]
36. Hee-Chan, K.; Sang-Hyup, L.; Dong-Ju, K.; Jae-Woo, C. Photocatalytic Activity of 2,4,6-Trichlorophenol by TiO₂ Mesostructures: Effects of Surface Modification, Calcination Temperature and Initial pH. *Water Air Soil Pollut.* **2013**, *224*, 1459–1467. [[CrossRef](#)]
37. Rozov, K.; Berner, U.R.; Kulik, D.A.; Diamond, L.W. Solubility and thermodynamic properties of carbonate-bearing hydroxalite-pyroaurite solid solutions with a 3:1 Mg/(Al+Fe) mole ratio. *Clays Clay Miner.* **2011**, *59*, 215–232. [[CrossRef](#)]
38. Lavand, A.B.; Malghe, Y.S. Nano sized C-doped TiO₂ as a visible-light photocatalyst for the degradation of 2,4,6-trichlorophenol. *Adv. Mater. Lett.* **2015**, *6*, 695–700. [[CrossRef](#)]
39. Skrabal, P.M. *Spectroscopy: An Interdisciplinary Integral Description of Spectroscopy from UV to NMR*, 1st ed.; vdf Hochschulverlag AG an der ETZ Zurich: Zurich, Switzerland, 2012; Volume 1, pp. 216–224. ISBN 978-3-7281-3385-4.
40. Turchi, C.S.; Ollis, D.F. Mixed Reactant photocatalysis: Intermediates and Mutual Rate Inhibition. *J. Catal.* **1989**, *119*, 483–496. [[CrossRef](#)]
41. Lin, Z.R.; Zhao, L.; Dong, Y.H. Quantitative characterization of hydroxyl radical generation in a goethite-catalyzed Fenton-like reaction Author links open overlay panel. *Chemosphere* **2015**, *141*, 7–12. [[CrossRef](#)]
42. Fu, S.; Deng, B.; Ma, D.; Cheng, H.; Dong, S. Visible-Light-Driven Photocatalytic Fuel Cell with an Ag-TiO₂ Carbon Foam Anode for Simultaneous 4-Chlorophenol Degradation and Energy Recovery. *ChemEngineering* **2018**, *2*, 20. [[CrossRef](#)]
43. An, X.; Liu, H.; Qu, J.; Moniz, S.J.A.; Tang, J. Photocatalytic mineralisation of herbicide 2,4,5-trichlorophenoxyacetic acid: Enhanced performance by triple junction Cu-TiO₂-Cu₂O and the underlying reaction mechanism. *New J. Chem.* **2015**, *39*, 314–320. [[CrossRef](#)]
44. Nosaka, Y.; Nosaka, A.Y. Generation and Detection of Reactive Oxygen Species in Photocatalysis. *Chem. Rev.* **2017**, *117*, 11302–11336. [[CrossRef](#)]
45. Chen, F.; Yang, Q.; Pehkonen, S.O.; Ray, M.B. Modeling of Gas-Phase Photodegradation of Chloroform and Carbon Tetrachloride. *J. Air Waste Manag. Assoc.* **2004**, *54*, 1281–1292. [[CrossRef](#)] [[PubMed](#)]

46. Rodríguez, E.M.; Márquez, G.; Tena, M.; Álvarez, P.M.; Beltrán, F.J. Determination of main species involved in the first steps of TiO₂ photocatalytic degradation of organics with the use of scavengers: The case of ofloxacin. *Appl. Catal. B* **2015**, *178*, 44–53. [[CrossRef](#)]
47. Wu, W.; Liang, S.; Chen, Y.; Shen, L.; Zheng, H.; Wu, L. High efficient photocatalytic reduction of 4-nitroaniline to p-phenylenediamine over microcrystalline SrBi₂Nb₂O₉. *Catal. Commun.* **2012**, *17*, 39–42. [[CrossRef](#)]
48. Xian, T.; Yang, H.; Di, L.; Ma, J.; Zhang, H.; Dai, J. Photocatalytic reduction synthesis of SrTiO₃-graphene nanocomposites and their enhanced photocatalytic activity. *Nanoscale Res. Lett.* **2014**, *9*, 1–9. [[CrossRef](#)] [[PubMed](#)]
49. Liu, W.; Wnag, M.; Xu, C.; Chen, S.; Fu, X. Significantly enhanced visible-light photocatalytic activity of g-C₃N₄ via ZnO modification and the mechanism study. *J. Mol. Catal. A Chem.* **2013**, *368*, 9–15. [[CrossRef](#)]
50. Mascolo, G.; Mascolo, M.C. On the synthesis of layered double hydroxides (LDHs) by reconstruction method based on the “memory effect”. *Microporous Mesoporous Mater.* **2015**, *214*, 246–248. [[CrossRef](#)]
51. Kim, B.K.; Gwak, G.H.; Okada, T.; Oh, J.M. Effect of particle size and local disorder on specific surface area of layered double hydroxides upon calcination-reconstruction. *J. Solid State Chem.* **2018**, *263*, 60–64. [[CrossRef](#)]
52. Teodorescu, F.; Paladuta, A.M.; Pavel, O.D. Memory effect of hydrotalcites and its impact on cyanoethylation reaction. *Mater. Res. Bull.* **2013**, *48*, 2055–2059. [[CrossRef](#)]
53. Czaplicka, M. Photo-degradation of chlorophenols in the aqueous solution. *J. Hazard Mater.* **2006**, *134*, 45–59. [[CrossRef](#)]
54. Xu, L.; Wang, J. Degradation of 2,4,6-trichlorophenol using magnetic nanoscaled Fe₃O₄/CeO₂ composite as a heterogeneous Fenton-like catalyst. *Sep. Purif. Technol.* **2015**, *149*, 255–264. [[CrossRef](#)]
55. Odling, G.; Robertson, N. Bridging the gap between laboratory and application in photocatalytic water purification. *Catal. Sci. Technol.* **2019**, *9*, 533–545. [[CrossRef](#)]
56. Guo, Q.; Zhou, C.; Ma, Z.; Ren, Z.; Fan, H.; Yang, X. Elementary Chemical Reactions in Surface Photocatalysis. *Annu. Rev. Phys. Chem.* **2018**, *69*, 451–472. [[CrossRef](#)]



© 2019 by the authors. Licensee MDPI, Basel, Switzerland. This article is an open access article distributed under the terms and conditions of the Creative Commons Attribution (CC BY) license (<http://creativecommons.org/licenses/by/4.0/>).